Advances in Industrial and Manufacturing Engineering 11 (2025) 100175

Contents lists available at ScienceDirect

Advances in Industrial and Manufacturing Engineering

journal homepage: www.sciencedirect.com/journal/advances-in-industrial-and-manufacturing-engineering

Laser directed energy deposition of FeSi/SS 316L advanced bimetallic high-speed rotors: From material characterization to performance evaluation

Chiara Gianassi [a,*], Erica Liverani [a], Andrea Cavagnino [b], Luca Zarri [c], Alessandro Ascari [a], Yulong Cui [b], Alessandro Fortunato [a]

[a] Department of Industrial Engineering (DIN), University of Bologna, Viale del Risorgimento, 2, 40136, Bologna (BO), Italy
[b] Department of Energy "G. Ferraris" (DENERG), Polytechnic of Turin, Corso Duca degli Abruzzi, 24, 10129 Torino (TO) , Italy
[c] Department of Electrical, Electronic, and Information Engineering "G. Marconi", University of Bologna, Viale del Risorgimento, 2, 40136, Bologna (BO), Italy

ABSTRACT

The demand for high-speed electric machinery has significantly increased, driving innovation in motor design. While permanent magnet rotors dominate due to their superior torque density and efficiency, their reliance on rare earth elements raises environmental and supply chain concerns. Synchronous Reluctance motors, which do not require permanent magnets, present a promising alternative, though their design limits rotor mechanical performance. Additive manufacturing, particularly Directed Energy Deposition (DED), addresses these challenges by enabling the production of multi-material structures.

This study investigates the potential of DED to fabricate high-speed rotors using $FeSi_{2.9}$, a soft magnetic alloy with high permeability, and the paramagnetic stainless steel AISI 316L. Single-material depositions were analyzed through microstructural and microhardness tests in both as-deposited and heat-treated conditions. Magnetic and mechanical characterization were performed on heat-treated samples. Annealing improved the magnetic properties of $FeSi_{2.9}$ without compromising the mechanical performance of AISI 316L. A bimetallic blank with alternating layers of the two materials was fabricated and characterized similarly. Subsequently, a rotor was extracted, machined, and tested.

Results demonstrated excellent printability, achieving crack-free deposits with >99 % relative densities. The fabricated SynRel rotor operated at speeds up to 100,000 rpm, underscoring the suitability of DED for producing advanced multi-material components for high-speed machinery.

1. Introduction

In recent years, the high-speed electric machinery industry has undergone substantial growth. In this field, permanent magnet (PM) motors are particularly important, thanks to their ability to operate in a wide speed range with high efficiencies (Gerada et al., 2014). Among the key alloys used for permanent magnets manufacturing, NdFeB guarantees high cost-performance efficiency, while SmCo is well known for its thermal stability at elevated temperatures (Cestone et al., 2024). However, these alloys contain rare earth elements (REEs), which are subject to significant price volatility and raise serious environmental and social risks related to their extraction and processing.

To address these concerns, the European Union has actively supported research initiatives aimed at reducing dependency on rare earth materials. One promising alternative is the development of Synchronous Reluctance (SynRel) motors that eliminates the need for permanent magnets. Despite its potential, the primary limitation of SynRel motors lies in the mechanical weakness of their rotor structures, which typically restricts their use to operating speeds below 20–30 krpm (Murataliyev et al., 2022). This limitation arises primarily from the internal flux barriers incorporated within the rotor design. Geometrically, these barriers manifest as distributed cuts in the cylindrical structure. Despite their essential role in enhancing magnetic performance, these cuts significantly compromise the rotor's mechanical stiffness.

In order to overcome this issue, advancements in metal additive manufacturing (MAM) have enabled the production of more complex designs and multi-material structures. For example, Newman et al. (2023) used Laser Powder Bed Fusion (LPBF) to fabricate bimaterial tensile specimens and toroids made of $FeSi_{3.5}$ and 316L stainless steel. Their work focused on material characterization for multi-metallic electric rotor development and led to the optimization of a four-pole rotor capable of achieving 55 krpm. This study demonstrated that additively manufactured rotors could overcome the speed limitations of conventionally produced counterparts. However, the common

---

* Corresponding author.
E-mail addresses: chiara.gianassi2@unibo.it (C. Gianassi), erica.liverani2@unibo.it (E. Liverani), andrea.cavagnino@polito.it (A. Cavagnino), luca.zarri2@unibo.it (L. Zarri), a.ascari@unibo.it (A. Ascari), yulong.cui@polito.it (Y. Cui), alessandro.fortunato@unibo.it (A. Fortunato).

https://doi.org/10.1016/j.aime.2025.100175
Received 30 June 2025; Received in revised form 26 September 2025; Accepted 5 November 2025

architecture of LPBF technology represents a constraint for efficient multi-material printing, due to the complex material changes which would be required.

Among the various metal additive manufacturing technologies, Directed Energy Deposition (DED) stands out for its versatility. Feenstra et al. (2021) provided a comprehensive review of DED applications, emphasizing its potential for fabricating bimetallic, functionally graded, and hybrid components. In particular, the production of layered hybrid materials remains a highly challenging but impactful strategy, despite the difficulties associated with the low resolution of DED processes. Although the topic is of great relevance, the available literature is limited. Chen et al. (2020) printed bimetallic specimens with alternating layers of 316L and Inconel 625, studying the phenomena occurring at the interface between the two materials from a thermodynamic and microstructural perspective. Li et al. (2019) conducted an experimental study using a hybrid manufacturing system that combined additive (DED) and subtractive (milling) processes to fabricate functionally bimetal materials composed by layers of Inconel 718 and AISI 316L. Their research focused on analyzing the properties in the transition zone between the different materials. While most studies have centered on applications involving dissimilar materials, such as iron-based and nickel-based alloys, Heer et al. (Heer and Bandyopadhyay, 2018) explored the properties of bimetallic structures composed of a non-magnetic (AISI 316) and a magnetic (AISI 430) steel. Their findings highlighted a gradual transition in both hardness and magnetic properties across the interface.

Building on these studies, Directed Energy Deposition technology enables the fabrication of components with alternating layers of different materials, offering simpler powder handling compared to LPBF. This characteristic makes DED a promising approach for the manufacturing of high-speed synchronous reluctance rotors. For high-speed applications (e.g., 100 krpm), flux barriers would need to be sufficiently thick, which could severely affect both magnetic and mechanical properties. DED offers a solution to this issue by substituting flux barriers with layers of paramagnetic material, thereby enhancing mechanical stiffness and expanding the operational speed range (Cui et al., 2024). Additionally, eliminating parasitic magnetic bridges improves the machine's saliency. Finally, the limitations associated with dimensional inaccuracies in DED can be addressed through subsequent machining operations.

Material selection is critical and must consider both functional properties and chemical compatibility. For magnetic materials, properties such as high permeability, high saturation magnetization, high electrical resistivity, and excellent thermal conductivity are essential (Lamichhane et al., 2020). However, these materials must also be compatible with DED processes. Iron-silicon alloys stand out as suitable soft magnetic materials for this application. Studies on LPBF (Zanni et al., 2022) and DED (Vyatskikh et al., 2023) have demonstrated that pure iron exhibits excellent printability, achieving relative densities up to 99.7 %. The addition of silicon reduces eddy current losses but negatively impacts processability in laser-based additive manufacturing. Garibaldi et al. (2016) reported that $FeSi_{6.9}$ is prone to cracking and microstructural defects, whereas alloys with 2.5–3.5 wt% silicon represent a balanced compromise between printability and magnetic performance in both LPBF (Newman et al., 2023) and DED (Lee et al., 2024; Sun et al., 2022). For the flux barrier material, requirements include a magnetic permeability similar to that of air and mechanical properties comparable to the ferromagnetic material. Austenitic stainless steel 316L fulfils these criteria and is widely used in DED processes due to its excellent printability (Ascari et al., 2020; Gianassi et al., 2025; Xiao et al., 2023). Although studies on these materials in LPBF are well-documented, their application in DED for bi-material printing remains unexplored.

In this study, $FeSi_{2.9}$ and AISI 316L austenitic stainless steel powders were deposited using the Laser Directed Energy Deposition process. The magnetic and paramagnetic materials were subjected to the same heat treatment and characterized mechanically through tensile testing and microhardness measurements, as well as magnetically. Microstructural analyses, performed before and after annealing with optical and electron microscopy, evaluated the effects of the treatment on grain morphology and size. Following this characterization, a bimetallic blank consisting of alternating layers of the two materials was fabricated via DED. The blank was analyzed using optical microscopy, scanning electron microscopy, microhardness measurements, and tensile testing with Digital Image Correlation (DIC). A rotor was then machined from the blank to achieve its final geometry and subjected to centrifugal testing. Then, the assembled motor prototype has been also tested in no-load and load conditions to include the temperature effects, which increase stress, and electromagnetic forces that can involve additional mechanical issues with respect to the centrifugal spin tests. All the experimental results confirmed that the rotor could withstand speeds up to 100 krpm without experiencing any rotodynamic issues.

2. Materials and methods

2.1. Specimen production and heat treatment

The production of a bulk to extract the bimetallic rotor required the deposition of two materials, one paramagnetic and one ferromagnetic. Austenitic stainless steel (AISI 316L) powder was selected as the paramagnetic material and supplied by Heeger Materials Inc. (CO, US), with a particle size nominally included between 53 and 150 μm. The soft magnetic material was a $FeSi_{2.9}$ alloy with 2.9 wt% of silicon produced by m4p Material Solutions GmbH (Austria), with powder particle size ranging from 45 to 106 μm.

Powder analysis was conducted using a scanning electron microscope (SEM) coupled with an EDS system for micro-elemental analysis. For both materials, a powder sample was analyzed to assess the chemical composition and particle size distribution through image analysis. The distribution data, represented in terms of relative and cumulative frequency, are shown in Fig. 1 along with Field Emission Scanning Electron Microscope (FESEM) images of the two powder samples. The chemical composition results obtained from the EDS analysis are provided in Table 1.

The initial phase of the experimental campaign focused on the separate deposition and characterization of the two materials, with the aim of determining their mechanical, magnetic, and microstructural properties. Subsequently, a bimetallic component consisting of alternating layers of $FeSi_{2.9}$ and AISI 316L was fabricated and characterized following the same steps. The substrate chosen for single-material depositions was a Fe plate with >99.95 % purity and 15 mm thickness. The choice of an extra-soft steel substrate as the base material was intended to minimize the carbon content, thereby reducing the risk of surface hardening caused by exposure to the concentrated thermal energy of the laser beam.

The fabrication process employed a Directed Energy Deposition system equipped with a 6-axis ABB IRB 4600 robotic arm. The system included a Laserline LDF-4500-60 diode laser with a maximum power output of 4.5 kW, delivered through a 600 μm core-diameter feeding fiber. Laserline OTS-5 focusing optics, with an 80 mm collimating focal length and a 300 mm focusing length, were used to achieve a spot diameter of 2.2 mm on the printing surface. Powder feeding was handled by a GTV PS2/2 system and a GTV PN6625 six-outlet nozzle, with a standoff distance of 25 mm and a powder jet focus of 2 mm. Argon was used as both the carrier gas (8 $l \cdot min^{-1}$ flow rate) and the shielding gas (20 $l \cdot min^{-1}$ flow rate).

For both materials, the following geometries were deposited:

- A six-layers specimen (30 × 40 mm^2) for microstructural characterization and microhardness testing. The scanning strategy involved firstly the deposition of the contour, followed by a zig-zag infill pattern with a 50 % overlap between tracks. Each subsequent layer

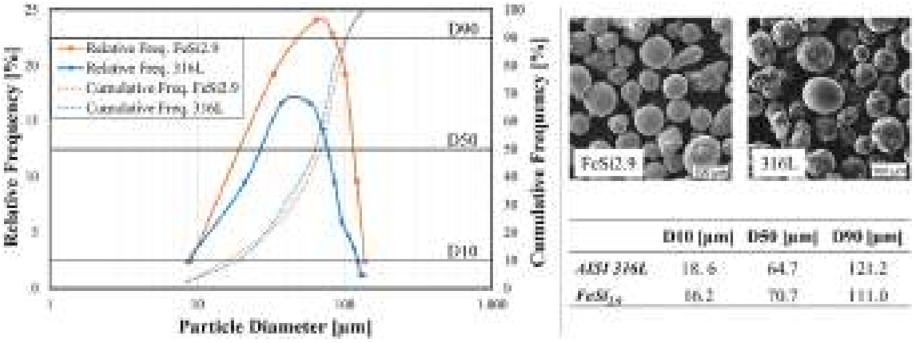

	D10 [µm]	D50 [µm]	D90 [µm]
AISI 316L	18.6	64.7	121.2
FeSi$_{2.9}$	16.2	70.7	111.0

Fig. 1. Particle size distribution and FESEM images of the powders for both FeSi$_{2.9}$ and 316L.

Table 1
Chemical composition of the particles of FeSi$_{2.9}$ and AISI 316L evaluated through FESEM-EDS.

[wt %]	Fe	Si	Cr	Mn	Ni	Mo
AISI 316L	bal.	1.15	17.21	1.65	10.55	2.39
FeSi$_{2.9}$	bal.	3.36	–	–	–	–

was rotated 90° relative to the previous one, alternating the starting point of deposition and the infill direction.

- Two parallelepiped blanks (30x90 × 10 mm^3) to be used for cutting tensile specimens, employing the same scanning strategy as the microstructural samples.
- Two toroidal blanks with an inner diameter of 65 mm, an outer diameter of 85 mm, and a height of 15 mm, designed to extract ring specimens for magnetic characterization. A concentric scanning strategy with a random starting point for each layer was chosen to prevent inhomogeneous material buildup.

The deposition of the bimetallic blank (55 × 128 mm^2 area) was performed on an AISI 316L plate with a thickness of 25 mm. The total deposition height was 55 mm, consisting of nine alternating layers of FeSi$_{2.9}$ and 316L. The required thickness of each layer, reported in Fig. 2, was determined through a FEM-based process optimization outlined in (Cui et al., 2024). The parallelepiped was deliberately oversized

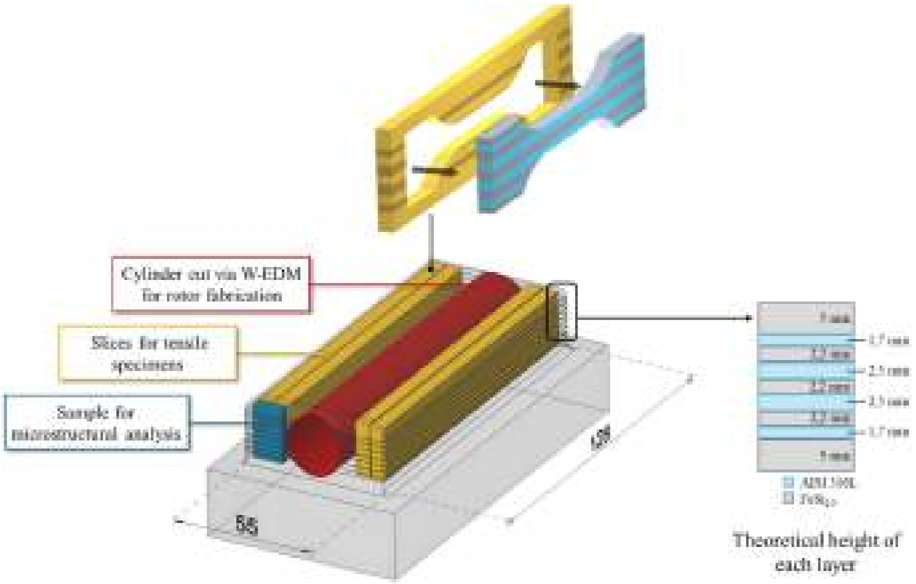

Fig. 2. Schematic of the bimetallic blank and the geometries extracted from it. On the right, diagram of the layer arrangement with their corresponding theoretical heights. On the top, a sketch illustrates how the tensile specimens were extracted from the slices.

Table 2
List and description of single material (1–3) and bimetallic (4) printed geometries.

#	Description	Quantity	Infill Strategy	Geometry	Heat treated
1	Sample for OM-SEM analysis	1[a]	Zig-zag pattern, 0/90°	Parallelepiped 30 × 40 mm, 6 layers	½ yes, ½ no
2	Bulk for tensile specimens	2[a]	Zig-zag pattern, 0/90°	Parallelepiped 90x30xh10 mm	Yes
3	Bulk for magnetic tests	2[a]	Concentric	Toroid, $D_{ext\text{-}int}$ = 85-65 mm, h = 15 mm	Yes
4	Bimetallic blank for rotor, tensile specimens and OM-SEM analysis	1	Zig-zag pattern: 90° for FeSi$_{2.9}$, 0/90° for AISI 316L	Parallelepiped 55x128xh55 mm, 9 levels of alternating materials	Yes

[a] Quantity for each material.

compared to the rotor to allow for the extraction of four tensile specimens and one sample for metallographic analysis, as shown in Fig. 2. For clarity, the scanning strategies and the deposited geometries are summarized in Table 2.

The process parameters used to fabricate both the single-material geometries and the bimetallic blank are reported in Table 3. In order to avoid excessive energy concentration, the laser power was progressively reduced as the number of deposited layers increased. In the second column, the first value represents the initial power, the second indicates the final power and the third specifies the power reduction per layer.

The table also includes the specific energies (E), calculated using the following formula:

$$E = \frac{P}{v \cdot D} \tag{1}$$

where P is the laser power, v is the scan velocity and D is the laser spot diameter (2.2 mm). The calculation was performed using the maximum value of laser power.

The process parameters for AISI 316L were optimized in previous studies (Ascari et al., 2020), and similar settings were adopted for $FeSi_{2.9}$. The resulting specific energy values align with those reported by (Vyatskikh et al., 2023; Sun et al., 2022) for pure Fe and $FeSi_{2.5}$ fabricated using DED technology.

For the purpose of multi-material application, the same heat treatment was applied to $FeSi_{2.9}$, AISI 316L, and bimetallic blank, with the primary aim of improving the magnetic properties of $FeSi_{2.9}$. A literature review focused on finding the optimal annealing parameters for $FeSi_{2.9}$, followed by an assessment of the treatment's effect on AISI 316L to ensure compatibility within the bimetallic system. The annealing of $FeSi_{6.9}$ was investigated by Garibaldi et al. (2018) on Laser Powder Bed Fusion specimens, testing temperatures between 400 °C and 1150 °C. The study revealed that magnetic permeability increased with higher annealing temperatures; however, significant grain growth observed at 1150 °C could adversely affect mechanical properties. Similarly, Lee et al. (2024) studied the annealing treatment on $FeSi_{3.5}$ produced via Directed Energy Deposition, confirming that elevated temperatures enhanced magnetic performance. Zanni et al. (2022) selected an annealing temperature of 850 °C for LPBF-fabricated pure Fe in order to prevent the α-Fe to γ-Fe phase transition, which occurs above 911 °C. Regarding AISI 316L, Xiao et al. (2023) showed that annealing DED-fabricated samples at 850 °C effectively reduced residual stresses. Based on these studies, an annealing treatment at 850 °C for 1 h, followed by air cooling, was adopted for both $FeSi_{2.9}$ and AISI 316L.

In order to evaluate the influence of the heat treatment, samples were divided into two parts: one half was analyzed in the as-built condition, while the other was subjected to heat treatment, along with other single-material and bimetallic blanks, for subsequent microstructural analysis.

2.2. Microstructural analysis and hardness tests

For microstructural analysis, a consistent procedure was adopted for AISI 316L, $FeSi_{2.9}$ (including as-built and heat-treated samples) and the bimetallic specimen. Metallographic samples were prepared by cutting cross-sections from each deposition using Wire-EDM. The sections were mounted and ground with progressively finer SiC sandpapers, followed by polishing with 1 μm alumina. Zeiss AXIO Observer A1m optical microscope was used for initial defect assessment and relative density calculations. The polished samples were chemically etched to reveal the microstructure: Nital was used for $FeSi_{2.9}$ and Vilella's reagent for AISI 316L, with swab times of 10 s and 45 s, respectively. To further highlight grain morphology in the bimetallic specimen, electrolytic etching with Ferric Chloride ($FeCl_3$) was applied at 2.5 V and 8 A for 10 s. The etched samples were examined using a high-resolution optical microscope (Keyence VHX-7000) and a scanning electron microscope (Tescan Mira3 with a Schottky emitter) equipped with an EDS probe. X-ray diffraction (XRD) analysis was performed on the bimetallic sample to identify the main phases and possible intermetallic compounds, using a Bruker D8 Advance diffractometer equipped with a Cu Kα radiation source ($\lambda = 1.5418$ Å).

Finally, Vickers microhardness tests were conducted using a Remet HX-1000 microdurometer, applying a 0.2 kg (HV0.2) load for a dwell time of 10–15 s, in accordance with ISO 6507–1:2023. For each specimen, measurements were taken all along a vertical path in the middle of the deposition, following the growth direction, with indentations spaced 0.5 mm apart.

2.3. Mechanical characterization

For both ferromagnetic and paramagnetic materials, two tensile specimens were extracted from oversized rectangular blocks fabricated using DED. After heat treatment, the specimens were cut to the geometry shown in Fig. 3a using W-EDM. Similarly, for the bimetallic tensile characterization, four specimens were extracted from slices of the printed blank, following the geometry illustrated in Fig. 3b.

Quasi-static tensile tests were performed for both single-material and bimetallic specimens in compliance with BS EN ISO 6892. These tests were conducted using a hydraulic testing machine (Italsigma, Forlì, Italy) equipped with a 20 kN load cell. The crosshead separation rate was maintained at a constant 0.17 $mm \cdot min^{-1}$, and strain measurements were obtained using an extensometer with a 25 mm gauge length. For each test, engineering stress-strain curves were generated, enabling the determination of the 0.2 % proof stress ($Rp_{0.2}$), ultimate tensile strength (UTS), and maximum strain ($\varepsilon_{\%}$). SEM images of the fracture surfaces were captured to analyze the failure characteristics.

For bimetallic specimens only, additional preparation was performed for 2D DIC (Digital Image Correlation) analysis. A random speckle pattern was applied to the surface under observation by first creating a white background and then spraying black paint dots. During the tensile tests of the bimetallic specimens, camera frames were captured at regular intervals of 200 ms, along with a corresponding data file containing load and displacement values for each frame. The camera used was a 6.4 MPx Basler acA3088-57 μm. To ensure proper illumination of the setup, two LED strips were mounted on a support behind the camera.

2.4. Magnetic characterization and prototype testing

For the magnetic characterization, two toroidal samples were extracted for each material from the annealed deposited bulks. Samples were machined by turning to achieve inner and outer diameters of 80 mm and 70 mm, respectively, and 4 mm thickness. Each toroid was wound with a magnetizing coil of 110 turns and a sensing coil of 40 turns. The specimens were tested in compliance with the EN IEC 60404–6:2018 standard, utilizing a custom test bench and data acquisition system developed by the authors, as described in (Cavagnino

Table 3

Process parameters employed for single material and bimetallic printing.

	Scan velocity v [$mm \cdot min^{-1}$]	Laser power P [W]	Powder flow rate g [$g \cdot min^{-1}$]	Layer height Δz [mm]	Specific energy E [$J \cdot mm^{-2}$]
AISI 316L	1020	2200–2000 – 80	9.1	0.7	58.8
$FeSi_{2.9}$	1200	2000–1800 – 80	10	0.8	45.5

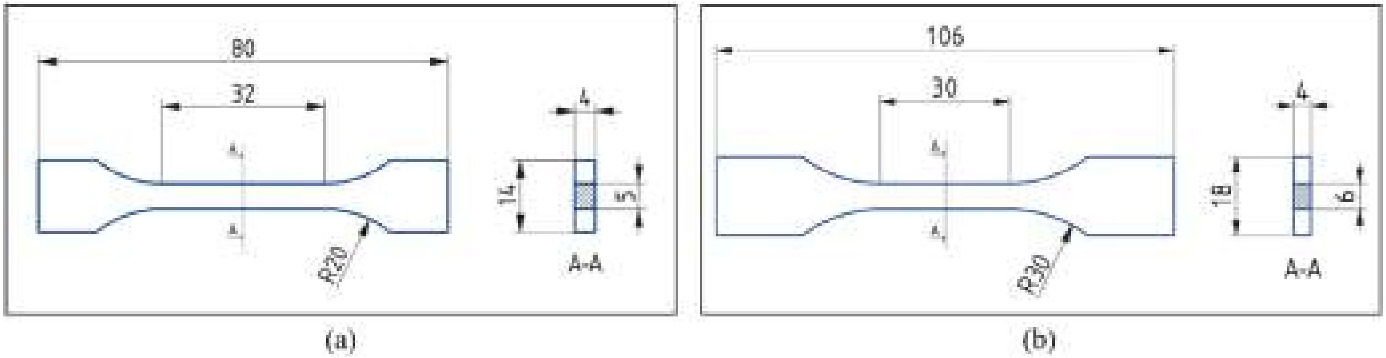

Fig. 3. Dimensional drawings of the tensile specimens for (a) single material and (b) bimetallic tests.

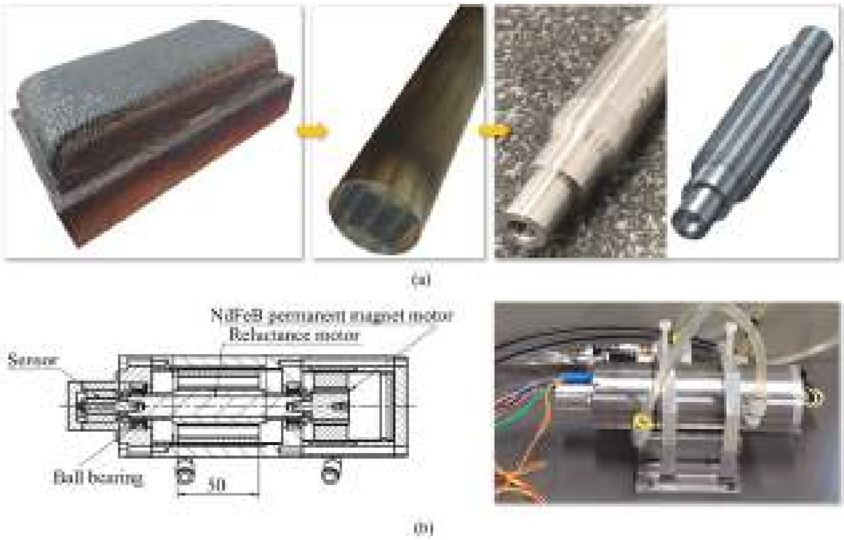

Fig. 4. Fabrication steps of the bi-metallic rotor produced using DED technology (a) and the developed test bench for testing the high-speed synchronous reluctance motor (b).

et al., 2023).

Fig. 4a shows how the printed rotor has been manufactured, starting from the cylinder cut from the printed blank sketched in Fig. 2. To test the high-speed synchronous reluctance motor prototype equipped with the printed bi-metallic rotor, a specific mechanical system has been designed and built – see Fig. 4b. In this system, a prime mover/brake synchronous permanent magnet machine is connected to one of the shaft ends, while a 130 krpm resolver (position and speed sensor) is mounted on the other end. The test rig is completed by a GaN-based three-phase power converter and a dSPACE controller board for rapid control prototyping (Testa et al., 2024).

3. Results and discussions

3.1. Microstructural characterization and microhardness tests

Fig. 5 shows optical microscope images of the cross sections used for relative density measurements. This analysis was made to ensure that the chosen process parameters did not lead to significant microstructural defects. The $FeSi_{2.9}$ sample exhibits fine, evenly distributed porosity throughout the deposition, achieving a relative density of 99.4 %. This result aligns with the values reported by (Vyatskikh et al., 2023) for DED-printed pure Fe. In contrast, for the SS 316L the porosity tends to be

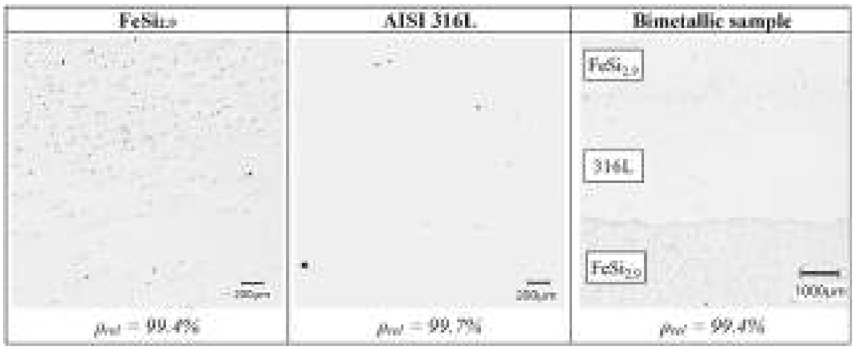

Fig. 5. Relative density and optical microscope images of $FeSi_{2.9}$, AISI 316L and bimetallic samples.

larger in size but much less widespread, resulting in an even higher density. Previous research on AISI 316L printing parameters (Ascari et al., 2020) indicates that high-density depositions can be achieved within a wide operating window, including power ranges of 1500–2200 W, speeds of 17–27 mm/s, and feed rates of 9.1–14.6 g/min. Conversely, Fe-Si alloys exhibit greater sensitivity to process parameters. Indeed, according to Sun et al. (2022), variations in power of just 500 W and speed of 4 mm/s in the printing of FeSi$_{2.5}$ can result in a lack-of-fusion rate ranging from 0.17 % to 2.16 %. In this work, both materials were printed without cracks, therefore the same parameters were applied to fabricate the multi-material blank. The bimetallic specimen revealed a relative density of 99.4 %; this result, together with the observed good adhesion between the layers and proper dilution at the interface, confirmed the reliability of the process parameters.

EDS analysis was conducted on a portion of the untreated FeSi$_{2.9}$ specimen, with the aim of revealing the Fe and Si distribution. The maps (Fig. 6a) indicate a uniform composition between grain interiors and boundaries, except for a few Si-rich particles randomly distributed, which suggests possible segregation phenomena. However, these particles are no longer observed after annealing, likely due to the dissolution of silicon into the solid matrix. This behavior aligns with findings by Garibaldi et al. (2018), who studied the effect of annealing treatment on FeSi$_{6.5}$.

Chemical etching of both treated and untreated FeSi$_{2.9}$ samples revealed three distinct microstructural zones (Fig. 6b). Near the interface, grain size is smaller with no preferential orientation due to rapid heat dissipation during deposition, which inhibits grain growth. In this region, the dilution with the Fe substrate limits the Si content at approximately 2 % both before and after heat treatment. Moving away from the interface, grains elongate into a columnar shape and grow perpendicular to the heat flow direction (Kurz et al., 2001), while Si increases to a maximum of 2.4 %. At the top of the deposition, the grains lose their preferential orientation and grow larger, forming an equiaxed structure. Fig. 6c shows high-magnification images of spherical defects in the treated sample. EDS analysis identifies their composition as consistent with the surrounding matrix except for minor traces of Al, likely residue from alumina polishing. The spherical shape, together with the dimension and composition, suggests these defects are unmelted powder particles embedded in the solid matrix.

Although the annealing treatment does not alter the three-zone morphology, it leads to a general increase in grain size. This trend is shown in the pre- and post-annealing micrographs, in Fig. 7. As reported by Lee et al. (2024), annealing FeSi$_{3.5}$ at 900 °C relieves residual stresses and promotes grain growth; this positively impacts magnetic properties by reducing the concentration of grain boundaries that hinder demagnetization.

Fig. 8 presents the key findings from the microscopy analysis of as-is and annealed 316L stainless steel specimens. Since the heat treatment produced no significant changes in the microstructure, both conditions were analyzed collectively. In Fig. 8a, the melt pools formed by laser passes are highlighted with dashed lines. Particularly, the pattern generated by alternating 90° rotation of the laser path between layers is clearly visible, aligning with the micrographs presented by Ribeiro et al. (2020) for the same scanning strategy. SEM images provide a view of the grain morphology. In the central region, the structure is predominantly columnar (Fig. 8b), transitioning to equiaxed grains near the top (Fig. 8c). Also (Zheng et al., 2008) observed a mixed microstructure with alternating zones of equiaxed, fine columnar, and coarse columnar grains. DED-printed austenitic stainless steel presents a dendritic structure, with the dendrites growing aligned with the isothermal gradient. In

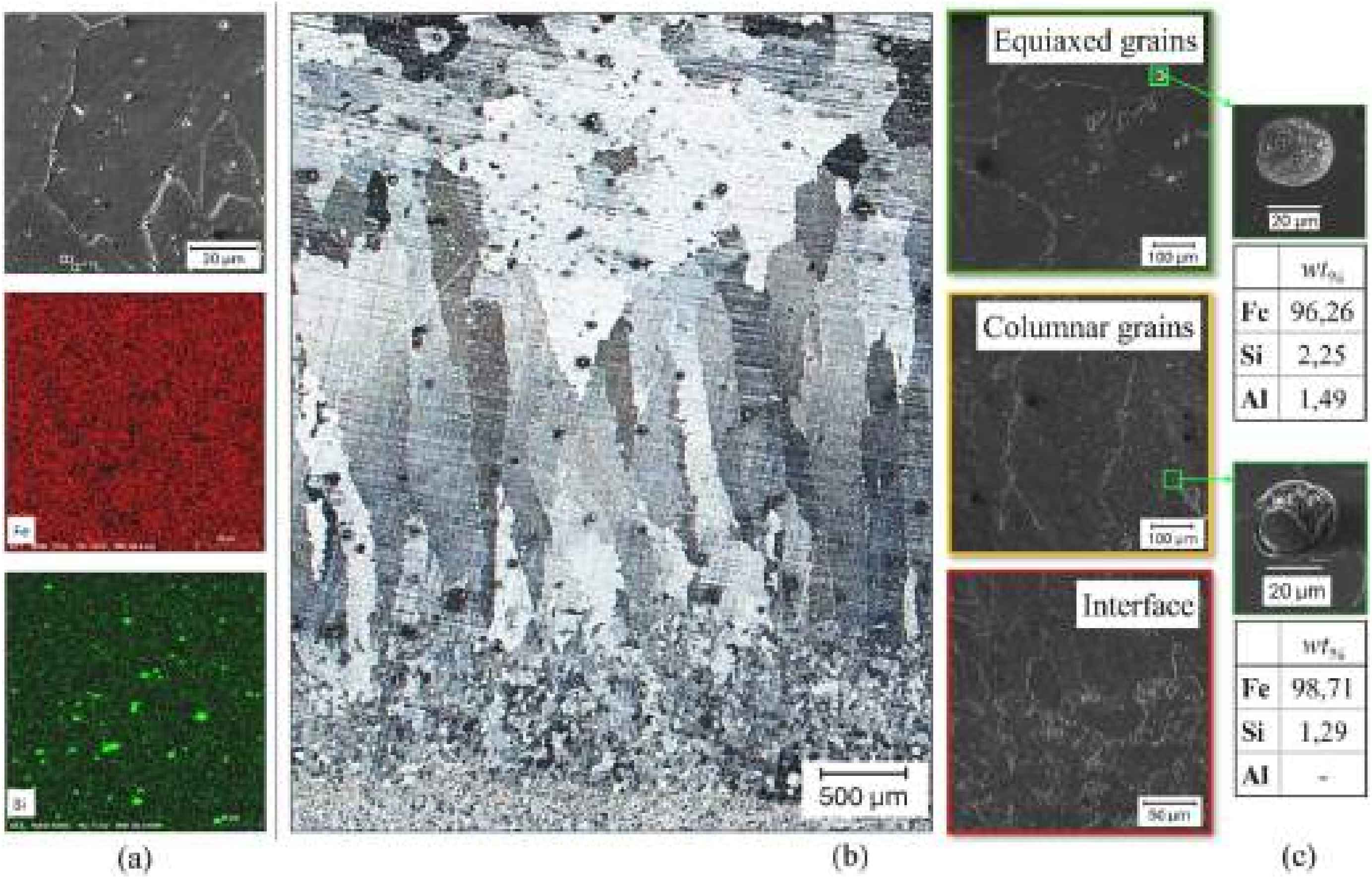

Fig. 6. EDS maps of untreated FeSi$_{2.9}$ (a); SEM and OM images of the grain morphology of the annealed FeSi$_{2.9}$ (b); high-magnification SEM images of defects with composition analysis (c).

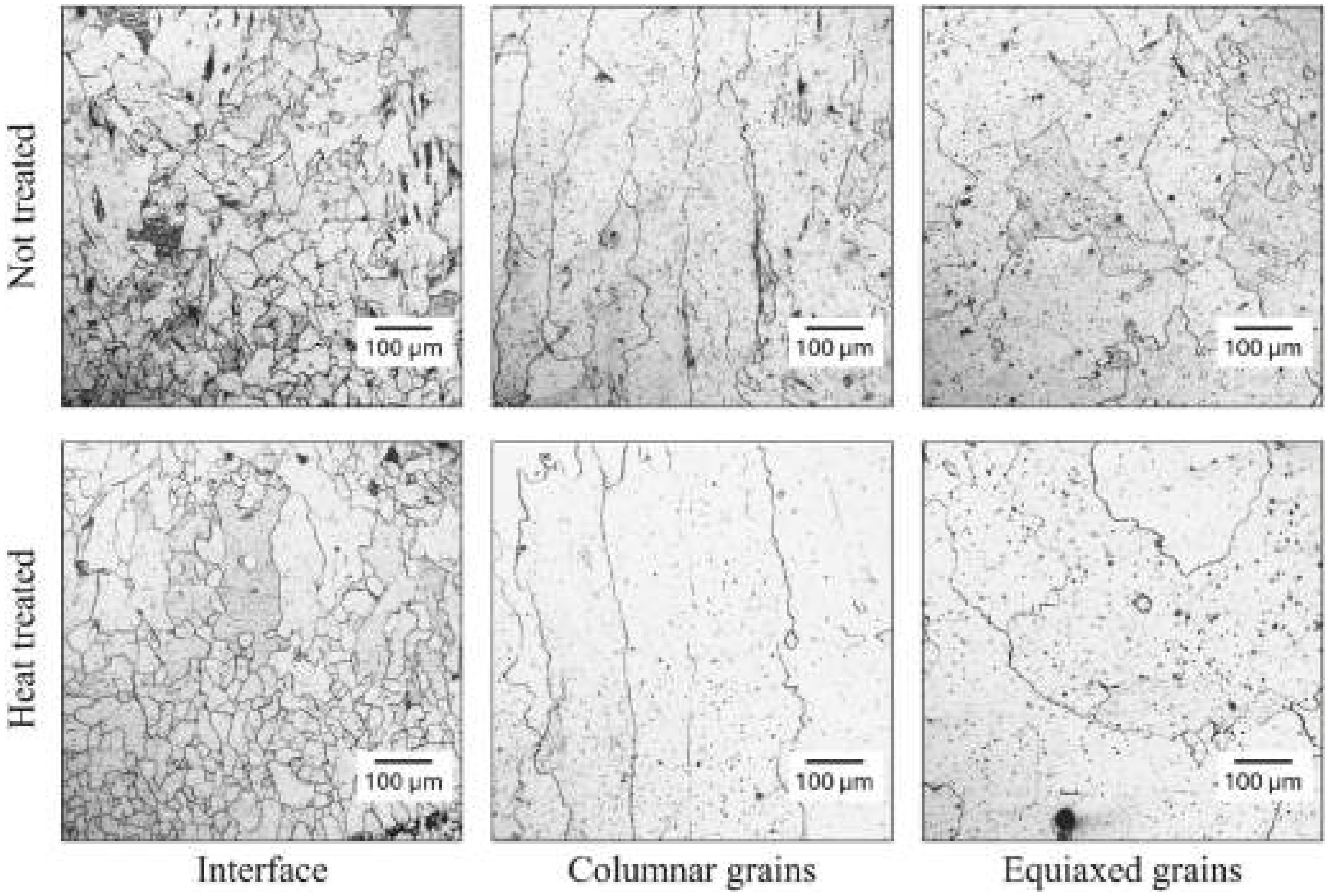

Fig. 7. Grain morphology of $FeSi_{2.9}$ before and after annealing in the three regions of the specimens.

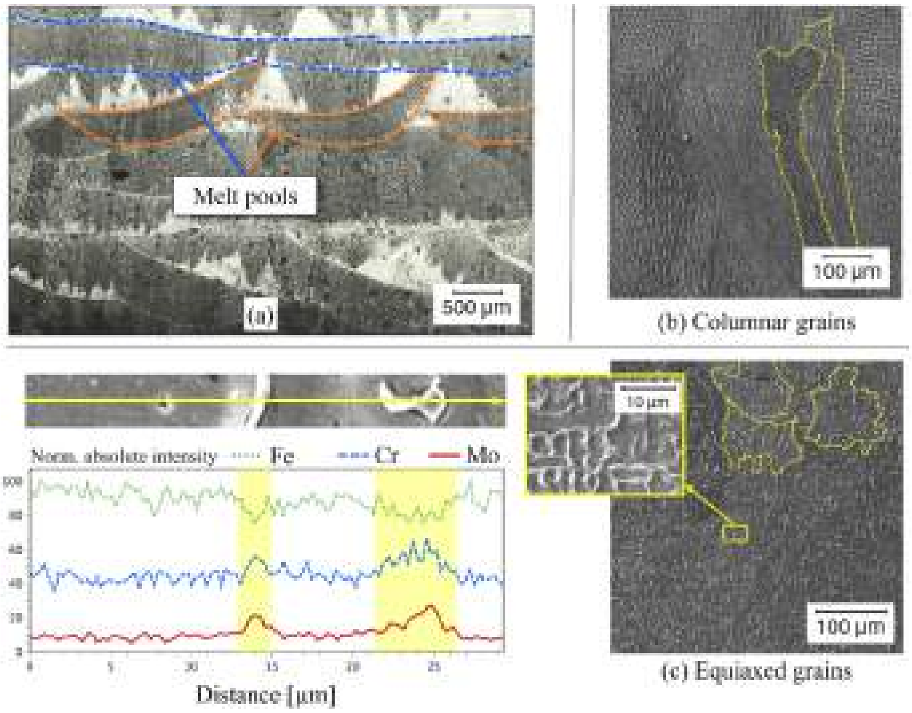

Fig. 8. Optical micrograph of the melt pools formed by laser passes in AISI 316L (a); SEM images of columnar grains (b) and equiaxed grains (c) with high magnification EDS analysis.

316L, the dominant phase is formed by austenite cells with intercellular ferrite. EDS analysis of dendritic structures revealed Cr and Mo enrichment in the intercellular regions, as highlighted in Fig. 8c, likely due to solidification front dynamics that limited full element incorporation into the dendrites.

The Vickers microhardness test results for annealed and as-is FeSi$_{2.9}$ and 316L specimens are summarized in Fig. 9. The values are reported both as a function of the distance from the substrate (Fig. 9a) and as a comparison between the average values of the four experimental conditions (Fig. 9b). Both materials exhibit a consistent microhardness profile across the deposition height, with standard deviations below 10 HV even after heat treatment.

For AISI 316L in the as-built state, the average microhardness is 197 HV, aligned with results reported by (Ascari et al., 2020) using Rockwell hardness tests on DED-fabricated samples. Similarly, Xiao et al. (2023) observed a microhardness of 207 HV for as-built 316L, decreasing to 176 HV after annealing at 850 °C for 2 h.

The FeSi$_{2.9}$ sample exhibits an average microhardness of 205 HV in its untreated state. While no comparable studies are available for DED-printed FeSi$_{2.9}$, Lee et al. (2024) obtained a higher microhardness of 284 HV for FeSi$_{3.5}$, likely due to their higher silicon content. After heat treatment, a 14.6 % reduction in hardness is observed, aligning with the results of (Zanni et al., 2022) after applying the same heat treatment on LPBF-printed pure iron specimens. This trend could be attributed to the stress relief induced by annealing: the thermal process causes a decrease in dislocation density, thus reducing the strengthening effect associated with this mechanism. Furthermore, according to the Hall-Petch relationship, also grain growth contributes to the reduction in mechanical properties.

Fig. 10 shows the XRD pattern of the bimetallic specimen. The analysis reveals that the samples is mainly composed of austenite, ferrite and intermetallic compounds. Austenite is confirmed as the predominant phase, with the observed peaks matching those reported by (Liu et al., 2024; Xiao et al., 2023). According to (Lee et al., 2024), FeSi$_3$ alloys produced via DED predominantly form a disordered A2 BCC phase, with peaks matching those obtained in this experiment. Several intermetallic compounds were also detected, likely corresponding to Cr–Si and Mo–Si phases. The peaks assigned to Mo–Si intermetallics are consistent with those reported by (Yan et al., 2009).

Electrochemical etching primarily highlights the microstructure within the FeSi$_{2.9}$ layers. Specifically, FeSi$_{2.9}$ exhibits a columnar grain structure both in the layer adjacent to the substrate and in the central layers (Fig. 11b and d), alternating with 316L. However, near the interface with the substrate, the grains tend to be smaller and without preferred orientation, similar to what was observed in single-material samples (Fig. 11a). In the 316L layers, the melt pool morphology and dendrite growth, oriented perpendicular to the interface, are clearly visible (Fig. 11c).

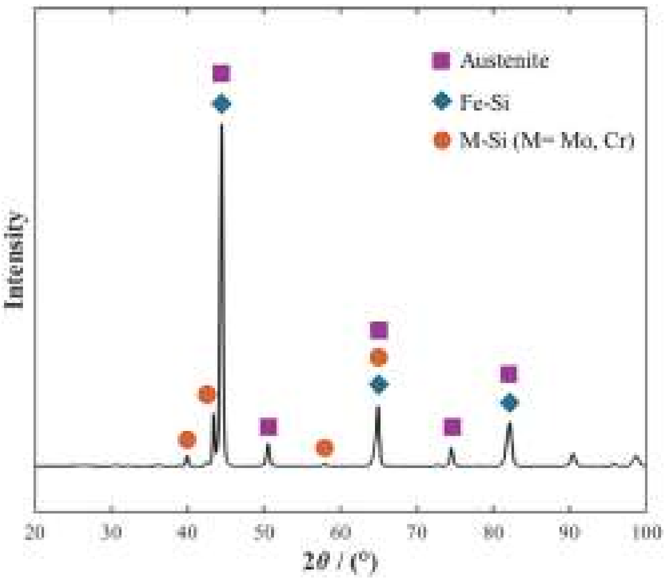

Fig. 10. XRD pattern of the bimetallic specimen.

At the transition zone between layers of different materials, both chemical etching (Fig. 12) and electrochemical etching (Fig. 11) reveal the melt pools of the overlying material when FeSi$_{2.9}$ is deposited beneath 316L. Chen et al. (2020) analyzed a DED-printed structure composed of alternating layers of dissimilar materials, identifying two types of interfaces depending on the material order. Specifically, the interface with AISI 316L above and IN625 below shares characteristics with the FeSi$_{2.9}$–316L configuration observed in this study, including visible melt pools of the upper material (Fig. 10), absence of epitaxial growth at the interface, and abrupt chemical composition changes, as shown in the EDS analysis (Fig. 12). Chen et al.'s simulations suggest a bidirectional material flow at the interface: counterclockwise flow promotes the formation of a “composite” zone from both materials, while clockwise flow drives the remelted lower material upwards, capturing it during solidification. Unlike Chen et al.'s multilayer structure, however, the materials alternated in this study do not exhibit significant

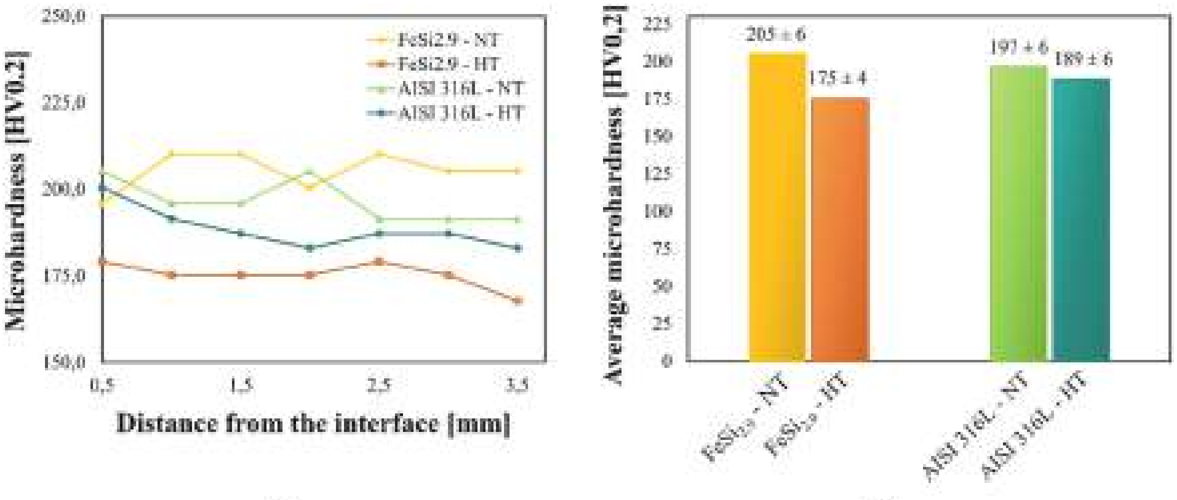

(a) (b)

Fig. 9. Vickers microhardness tests as a function of the distance from the substrate (a); average microhardness and standard deviations for each test condition (b).

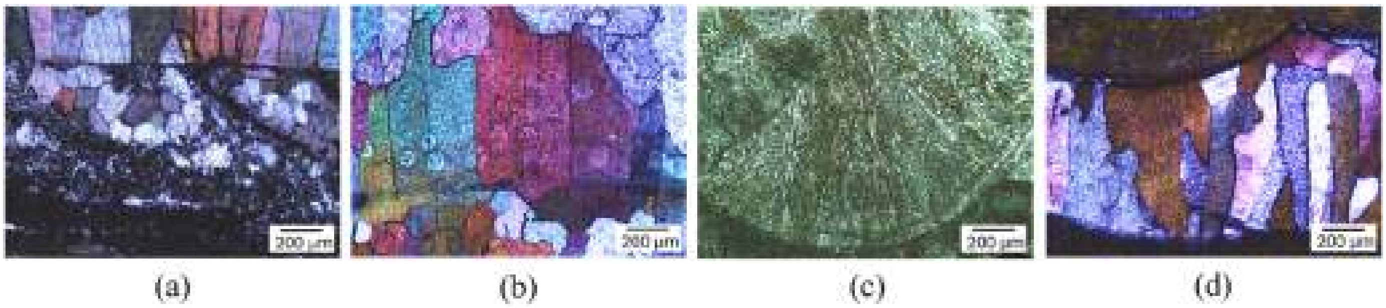

Fig. 11. Electrochemical etching of the bimetallic specimen: interface with the substrate (a), $FeSi_{2.9}$ columnar grains (b), AISI 316L melt pool shape (c) and internal $FeSi_{2.9}$ layer (d).

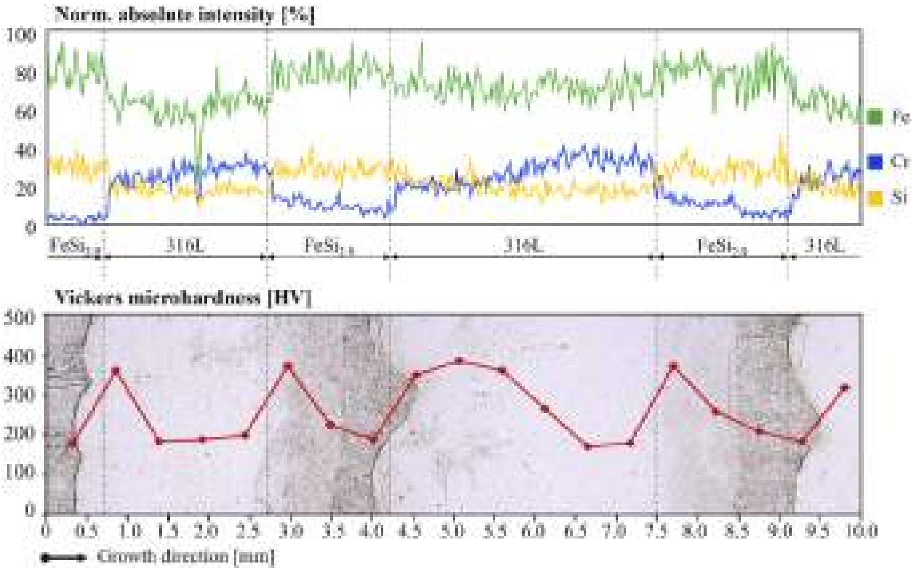

Fig. 12. Correlation between EDS analysis (Fe, Cr, and Si content) and microhardness measurements for the bimetallic sample, plotted as a function of the distance from the base material.

differences in density, viscosity, or chemical composition; therefore, although the transition zone is less evident in the configuration with 316L beneath and $FeSi_{2.9}$ above, it is reasonable to assume a similar interface. This hypothesis is supported by EDS analysis, which consistently indicates sudden compositional changes between layers, and by Fig. 11d, where the morphology of a central $FeSi_{2.9}$ layer and its corresponding interface is shown.

EDS analysis was performed along the entire height of the bimetallic blank, enabling the determination of the real deposited thickness of each material layer. These values were compared with nominal thicknesses in Table 4.

Excluding the first and last layers from the analysis, which were intentionally deposited in excess to facilitate the rough rotor cutting by EDM, the table shows that $FeSi_{2.9}$ exhibits less growth compared to 316L, which consistently reports a positive deviation from the theoretical values. The reduced height of the ferromagnetic layers compared to the theoretical design could potentially have a negative impact on the magnetic properties. Nonetheless, when comparing layers equidistant from the central one, it is observed that symmetry is maintained, with a maximum height difference of 0.1 mm. This ensures minimal disruption to the magnetic flux distribution within the rotor. It is worth mentioning that thickness inconsistency does not perturb the mechanical balance of the rotor, because the $FeSi_{2.9}$ and 316L materials have similar mass density. However, it can affect certain electromagnetic performances, such as the average torque and torque ripple. A possible strategy to mitigate this issue would be the adoption of a hybrid deposition–milling approach. In this case, after the deposition of each material layer, a milling operation could be performed to reach the desired thickness before depositing the subsequent layer, thus enabling layer-by-layer control of the geometry. Such an approach can be

Table 4
Comparison of theoretical and nominal layer heights for alternating materials, along with the percentage variation from the nominal values.

Layer Number	1	2	3	4	5	6	7	8	9
Theoretical [mm]	5.0	1.7	2.2	2.5	2.2	2.5	2.2	1.7	5.0
Real [mm]	5.6	1.9	1.4	3.0	1.6	2.9	1.5	1.8	5.6
Variation [%]	12.0	11.8	-36.4	20.0	-27.3	16.0	-31.8	5.9	12.0

■ $FeSi_{2.9}$ ■ AISI 316L

Table 5
Average microhardness and standard deviation for the $FeSi_{2.9}$, AISI 316L and interface regions in the bimetallic specimen.

	Average Microhardness [HV0.2]	Standard Deviation [HV0.2]
$FeSi_{2.9}$	220	31
AISI 316L	210	35
Transition zone	373	22

practically implemented using CNC milling machines equipped with a laser DED powder deposition head, allowing the entire process to be carried out in a single setup, with only a tool change required between deposition and milling.

For the bimetallic sample, Table 5 summarizes the average hardness values and standard deviations for three identified regions: $FeSi_{2.9}$, 316L, and the transition zones, which are analyzed independently of layer sequence due to the aforementioned observations. The results reveal a general increase in average hardness compared to single heat-treated materials, with the most significant increases – up to 77.6 % – occurring in the transition zone. Notably, the hardness peaks at the interfaces exhibit a relatively low standard deviation of 22 HV, indicating that the same strengthening mechanism operates consistently across all $FeSi_{2.9}$–316L interfaces. Similar increases in hardness at material transition zones were observed by Li et al. (2019) in a hybrid multilayer structure of 316L and IN718. The authors attributed the trend to the formation of chromium carbides and solid-solution strengthening from Cr dissolution into the face-centered cubic lattice of Ni. Despite Ni being present in only 10.5 % of the 316L alloy, a similar mechanism could occur also in this study, and Cr seems to play an important role in this strengthening phenomenon. Supporting this observation, Tanwar et al. (Tanwar and Jhavar, 2025) also reported increased hardness at the interface of a DED-deposited bimetallic structure composed of SS309 and SS316L, attributing it to the presence of chromium, which enhances the ferrite phase.

3.2. Mechanical characterization

The stress-strain curves from single-material tensile tests are shown in Fig. 13a, with the values summarized in Table 6. For clarity, one representative curve is displayed for each material. AISI 316L exhibited a maximum strain of 44.2 %, with failure occurring due to localized necking (Fig. 13a). SEM analysis of the fracture surfaces revealed dimples in the central region (Fig. 14a and b), which nucleate at internal discontinuities and grow under deformation until the material failure (Pineau et al., 2016). The presence of dimples and localized necking indicate a ductile fracture mechanism. Although the yield strength values are slightly below the average reported in the literature (Aversa et al., 2021), they remain consistent with the results from (Ascari et al., 2020). Conversely, the stress-strain response of $FeSi_{2.9}$ showed a distinctly brittle behavior, with a maximum fracture strain of 3.1 % and transgranular fractures. SEM images (Fig. 13c and d) suggest that cleavage is the predominant failure mechanism, characterized by fracture surfaces perpendicular to the direction of the maximum principal stress. Cleavage is commonly observed in ferritic steels (Pineau et al., 2016) and the brittle behavior may be enhanced by the presence of silicon within the alloy. The tensile and yield strength values for $FeSi_{2.9}$, listed in Table 6, align with those reported by Khan et al. (2013) for $FeSi_2$ fabricated via casting and cold rolling but are lower than those obtained for DED-printed $FeSi_{3.5}$ samples (Lee et al., 2024).

Fig. 13b presents the stress-strain curves obtained from the tensile tests on the bimetallic specimens. To ensure consistency between the

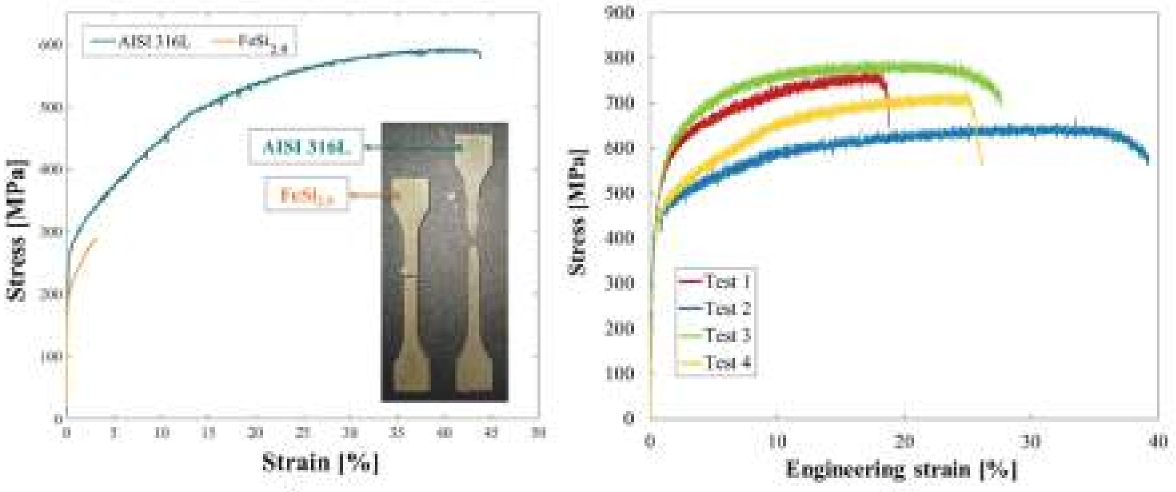

(a) (b)

Fig. 13. Stress-strain curves resulting from single material (a) and bimetallic (b) tensile tests.

Table 6
List of mechanical properties obtained from tensile tests.

Specimen	Yield strength $R_{P0.2}$ [MPa]	Ultimate tensile strength UTS [MPa]	Max strain ε_{ext} [%]	Max strain – DIC ε_{DIC} [%]
$FeSi_{2.9}$ – Test 1	215	255	1.1	–
$FeSi_{2.9}$ – Test 2	190	290	3.1	–
316L – Test 1	190	470	44.0	–
316L – Test 2	230	555	44.2	–
Bimetallic – Spec. 1	297	782	18.8	16.2
Bimetallic – Spec. 2	343	665	39.2	39.9
Bimetallic – Spec. 3	267	798	27.7	29.3
Bimetallic – Spec. 4	313	730	26.2	25.3

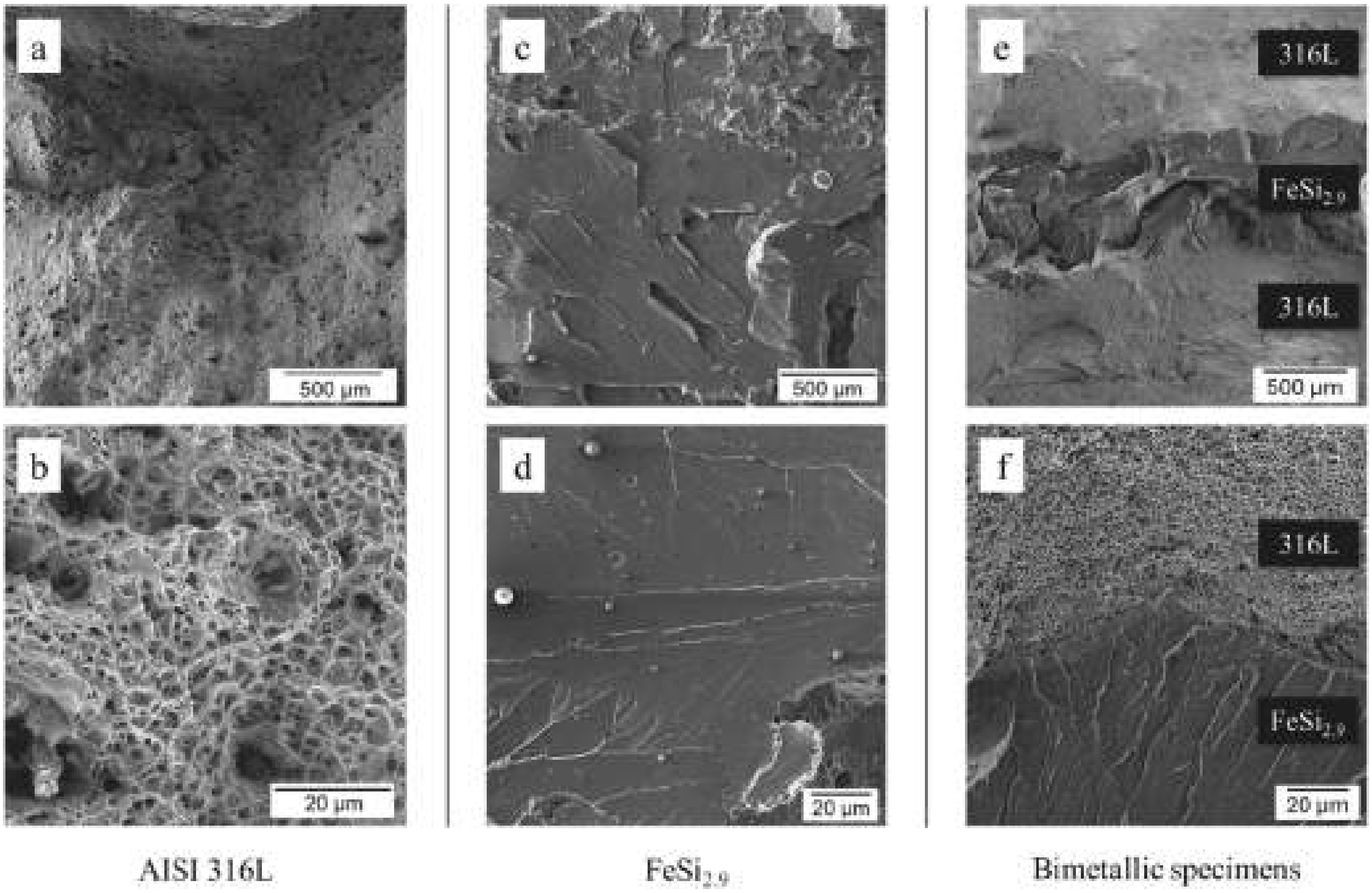

Fig. 14. SEM images of the fracture surfaces after tensile tests, at high and low magnifications.

measured values, both the maximum strain values obtained from the stress-strain curves and those calculated via Zeiss Correlate software from DIC analysis are reported in Table 6. An overall increase in both yield strength and ultimate tensile strength (UTS) is observed compared to the single-material tests, with fracture stresses reaching nearly 800 MPa and yield strength exceeding 300 MPa. This result contrasts with previous studies on bimetallic DED-printed specimens with vertical interfaces. For instance, Tanwar and Jhavar (Tanwar and Jhavar, 2025) produced multilayer structures in AISI 308 and AISI 316L using DED, but their specimens with vertical interfaces exhibited lower mechanical strength than the base materials. Similarly, Rajamani et al. (2025) tested tensile specimens with vertical layers of IN718 and 316L, finding intermediate strength and elongation values between the two constituents. The observed increase in tensile strength in our case is likely due to solid solution strengthening mechanisms occurring at the interface, which act as barriers to dislocation motion, locally enhancing strength. The more ductile material – AISI 316L in this case – could also serve as a barrier to crack initiation and propagation in the more brittle FeSi layer. Beyond strengthening, the localized hardness increase observed at the interfaces contributes positively to the overall tensile behavior. Indeed, if the interface between two materials with very different properties were weaker than the base materials, plastic deformation would accumulate in this region, making it a critical point and leading to premature failure at lower stress and strain levels. The presence of hardness peaks and good metallurgical bonding at the interface promotes a more uniform stress distribution, resulting in improved mechanical performance of the bimetallic specimen compared to the single-material ones. However, these peaks could be related to the intermetallics formation detected with XRD analysis, which could affect the mechanical properties of the bimetallic structure by promoting brittleness. All specimens exhibited ductile behavior, fracturing after necking, although the presence of brittle $FeSi_{2.9}$ layers led to lower elongations at break compared to AISI 316L specimens. However, a significant variation in strain values is observed across different tests: the minimum strain was recorded for specimen 1, below 20 %, whereas specimen 2 exhibited values approaching 40 %.

To investigate the origin of this discrepancy, a cross-section was extracted from each specimen, polished, and analyzed using optical microscopy to assess the layer arrangement within the gauge length. $FeSi_{2.9}$ can be identified by its darker appearance and more evident grain boundaries. These cross-sections were then correlated with the shear strain distribution (ε_{xy}) at break, which takes into account the effect of longitudinal (ε_{yy}) and transverse (ε_{xx}) strain components, aligned parallel and perpendicular to the loading direction, respectively (Fig. 15). Strain mapping helped to find shear stress concentrations, indicating the location of failure initiation. The figure also indicates the maximum values of ε_{yy} and ε_{xx} for each specimen.

As shown in the micrograph, specimen 1 contains two $FeSi_{2.9}$ layers, unlike the other specimens, which have only one. The higher proportion of the brittle FeSi in this specimen explains the lower strain values in both directions. Moreover, the shear strain distribution (ε_{xy}) highlights a stress concentration at the interface between the first 316L layer and $FeSi_{2.9}$, suggesting that crack initiation likely occurred in this region.

Conversely, specimen 2 exhibited the highest strain values in both the x and y directions. The micrograph reveals that the $FeSi_{2.9}$ layer is positioned centrally, while the strain map suggests a ductile fracture with crack initiation after localized necking. For specimens 3 and 4, the micrographs reveal a more inclined layer arrangement, attributed to the fact that these samples were extracted from the outermost regions of the multimaterial blank (Fig. 2). However, this misalignment does not

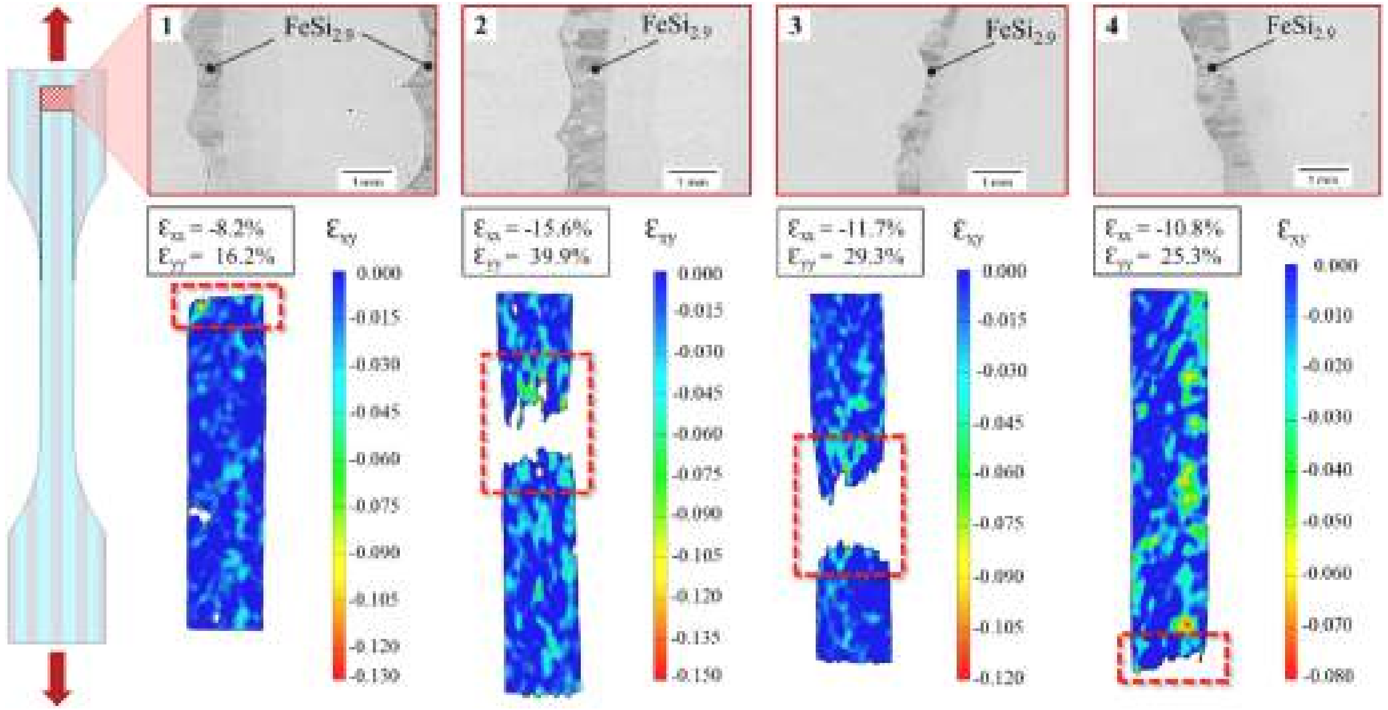

Fig. 15. Correlation between tensile specimens' cross sections and shear strain maps at break obtained with DIC analysis. For each specimen, also maximum strains in x and y directions are reported. Specimens 1 and 2 were extracted from central slices close to the rotor, while specimens 3 and 4 came from outer slices, where the layers are more inclined.

appear to significantly influence the mechanical behavior, as both specimens exhibit trends similar to the others, with intermediate strain values and predominantly ductile failure modes.

Jin et al. (2024) also studied strain distribution in bimetallic DED-printed specimens to analyze interfacial effects. While their analysis successfully identified fracture initiation points, they reported brittle failure in specimens with vertical material interfaces, contrary to our findings. This discrepancy is likely due to differences in deposition strategies: their study involved adjacent material deposition, whereas in the present work layers were stacked and the specimens were subsequently extracted horizontally. Notably, their horizontally layered specimens exhibited good adhesion and a ductile response, aligning with our results.

The fracture surfaces, exemplified in Fig. 14e–f, clearly illustrate the variation in fracture mechanisms across different layers: dimples are distinctly visible in the 316L regions, whereas brittle fracture features are concentrated in the central FeSi$_{2.9}$ layer. The transition between fracture mechanisms appears abrupt at the interface between the two materials, with Fig. 14f providing a magnified view where the melt pools of 316L are distinguishable.

For a more detailed analysis of the DIC results, specimen 3 is taken as a reference. As shown in Fig. 16, strain appears to be distributed across the entire specimen. Images reveal the tendency to form shear bands oriented at 45° in both directions, where deformation occurs preferentially. This behavior was consistently observed across all specimens, indicating that it is not related to the inclined layer arrangement found only in specimens 3 and 4. In ductile materials, plastic deformation tends to concentrate along maximum shear planes, oriented at 45° to the loading direction. Additionally, the difference in ductility between the two materials and the potential presence of residual stresses from thermal cycles may have influenced deformation patterns, promoting the formation of shear bands along preferred directions.

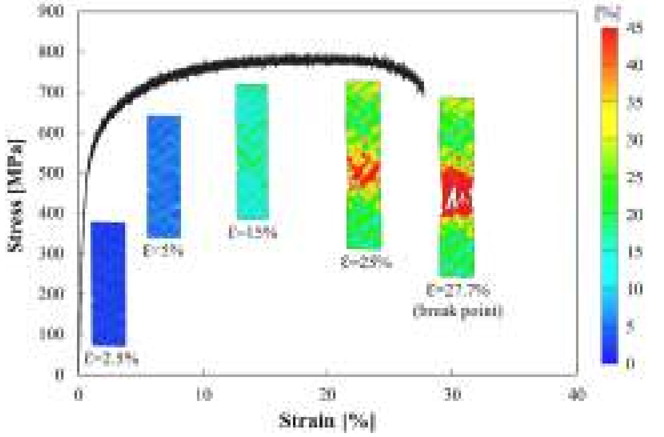

Fig. 16. Stress-strain curve of specimen #3 with DIC images at different ε_{yy} values.

3.3. Magnetic characterization and prototype testing

Fig. 17a presents the low-frequency BH curves for FeSi toroidal cores. For reference, the performance of a conventional FeSi laminated material (M270-35A), commonly used in stators, is also included.

The results indicate that while the magnetic performance of the DED-printed core remains below that of conventional laminated FeSi materials, it demonstrates promising characteristics for high-speed applications. Specific losses, as shown in Fig. 17b, are influenced by the inherent microstructural features and residual stresses of the DED process. For reference, studies on LPBF-printed FeSi alloys (Cavagnino et al., 2023) report slightly lower specific losses compared to DED, likely due to differences in grain structure and stress distribution. The hysteresis loops at 1 Hz for the DED-printed FeSi$_{2.9}$ core, presented in Fig. 17c, confirm the material's behavior under low-frequency excitation, highlighting its potential for application in magnetic components.

For SS 316L, the magnetic behavior was tested at 50 Hz (Fig. 17d). The test setup used in this study provides only an approximate

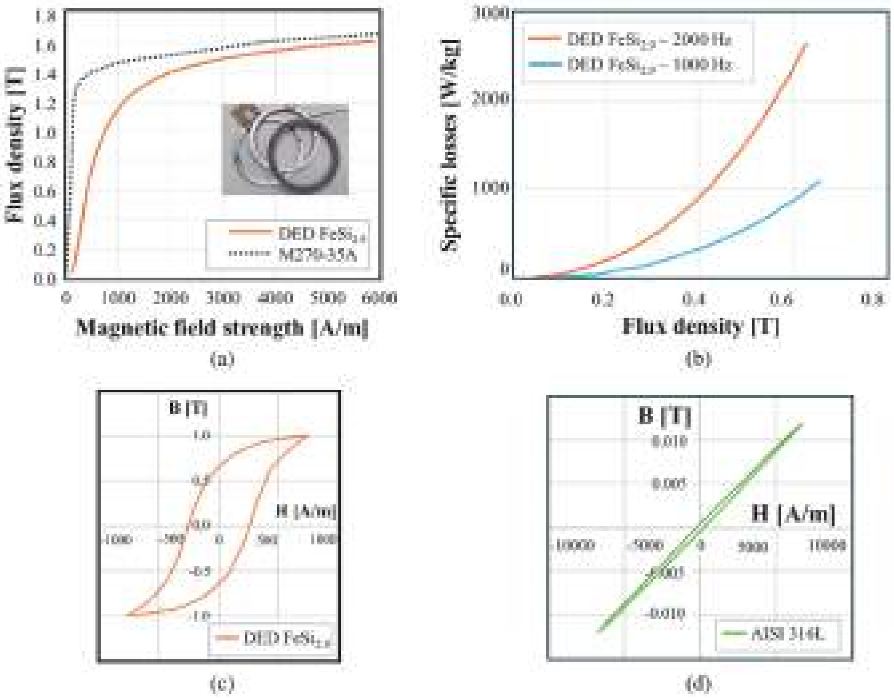

Fig. 17. Magnetic properties of DED-printed FeSi: magnetization BH curve at 1 Hz, including M270-35A for reference (a); specific losses for different excitation frequencies (b); hysteresis cycles at 1 T and 1 Hz (c). Hysteresis cycle for SS 316L (d).

indication of its magnetic response rather than precise measurements; however, a general trend in material response was identified. The hysteresis loop area, along with the associated losses, remains negligible at this frequency. The relative permeability can be calculated from the hysteresis cycle using the following linear equation:

$$B = 1.77 \cdot 10^{-6} \cdot H \tag{2}$$

The result is estimated at approximately 1.4. Although the literature typically reports a value of 1.02 (Credo et al., 2023), the estimated permeability aligns reasonably well with expected values, reinforcing the notion that annealed SS 316L maintains its paramagnetic behavior within the tested frequency range.

To evaluate the impact of the rotor material permeabilities on the rotor magnetic saliency, the inductance maps of the motor prototype have been measured at the rotational speed equal to 20000 rpm, in accordance to the procedure described in (Varvolik et al., 2022). Fig. 18 reports the comparison of the measured and FEM-computed inductance maps in the synchronous rotor reference frame (*d, q*), where the *d*-axis is the rotor symmetry axis with the highest magnetic permeance (i.e. parallel to the $FeSi_{2.9}$ layers), while the *q*-axis is the rotor symmetry axis perpendicular to the *d*-axis (i.e. along the direction of the minimum permeance).

The prototype is being tested using the mechanical test system shown in Fig. 4b. The bearings have been rodded and the rotor has been spun up to 100,000 rpm without any particular problems being observed. Fig. 19 shows the main signals measured under a step transient from 0 rpm to 100,000 rpm in no-load conditions with a slope limited to 5000 rpm/s. During the test, the switching frequency of the inverter is 40 KHz with a DC bus voltage of 350 V. The machine is operated with the maximum torque per ampere control strategy as the '*torque*' current is equal to the

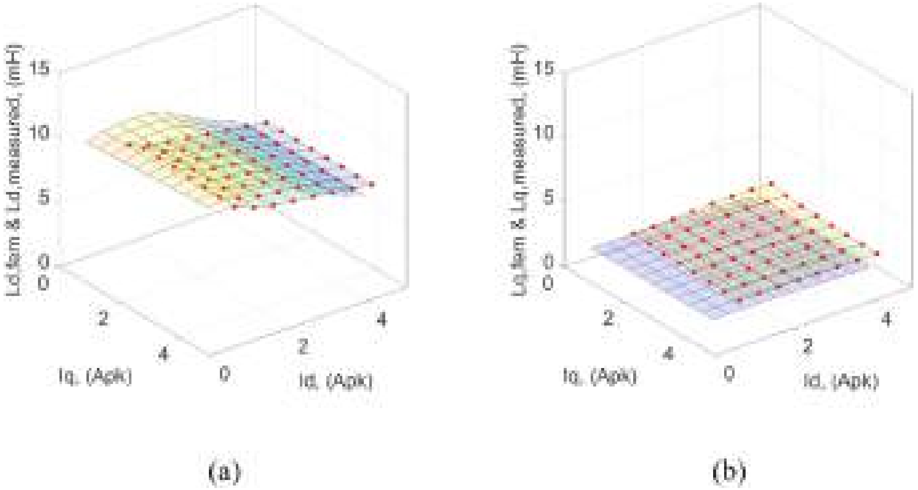

Fig. 18. Measured inductance maps (with red markers) compared with the FEM-based estimations, shown for the directions of maximum (a) and minimum (b) permeance.

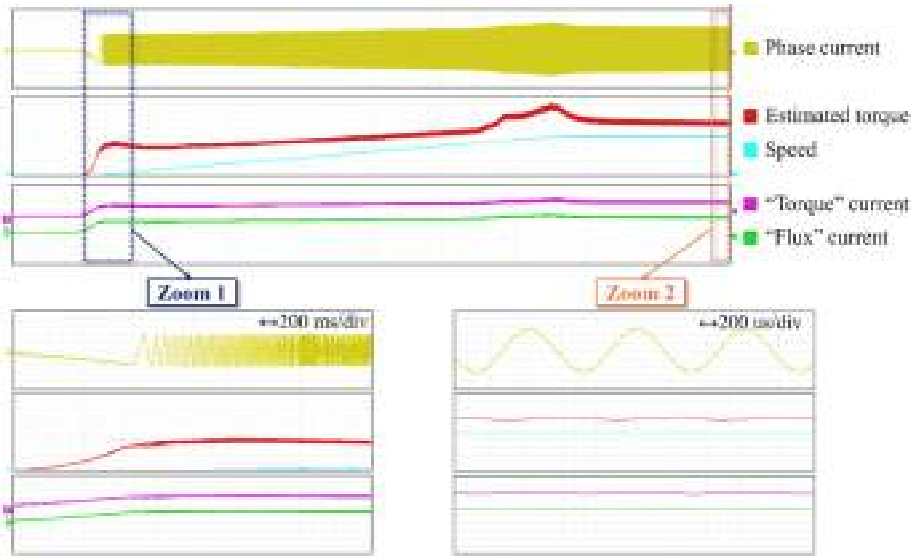

Fig. 19. Speed step response with setpoint at 100,000 rpm and ramp rate limiter of 5000 rpm/s. From the top: phase current (yellow ochre, 1 A/div), estimated torque (red, 5mNm/div), shaft speed (light blue, 20 krpm/div), d- and q axis currents (purple and green, respectively, 1 A/div).

'*flux*' current.

The measured inductance maps demonstrate that the relative permeability of AISI 316L is larger than that specified in the datasheets or in literature, and that the value measured with the toroidal sample could be considered reasonable or even slightly underestimated. Furthermore, the inductance maps demonstrate negligible saturation in the direction of minimum permeance (i.e. along the q-axis), as well as negligible magnetic cross-coupling between the two axes even at maximum current amplitudes. Finally, the measured inductance maps allowed estimating the performance of the motor prototype at the rated speed, torque and supply voltage, fully validating the electromagnetic design of the proposed high-speed anisotropic rotor. The expected input stator currents and electromagnetic torque have been measured in no-load conditions at the rated speed of 100000 rpm, further confirming that it is possible to produce anisotropic rotors using DED technology suitable for high-speed synchronous reluctance machines with specific performance up to 5 Nm/dm^3 and 50 kW/dm^3.

4. Conclusions

This study explored the potential of Laser Directed Energy Deposition technology for the fabrication of bimetallic high-speed rotors made from $FeSi_{2.9}$ and AISI 316L stainless steel, with a focus on their mechanical and magnetic performance. The main findings can be summarized as follows:

- Both $FeSi_{2.9}$ and 316L achieved high relative densities without cracks in single material printings and demonstrated good interfacial adhesion and proper dilution between the layers in the bimaterial deposition. $FeSi_{2.9}$ exhibited a columnar grain morphology, while 316L presented alternating columnar and equiaxed structures. Annealing increased grain size in $FeSi_{2.9}$, enhancing magnetic properties by reducing grain boundary concentration.
- The bimetallic specimens demonstrated improved mechanical properties compared to single-material samples, with yield strength and ultimate tensile strength up to 343 and 798 MPa, respectively. The interfaces acted as barriers to dislocation motion, contributing to solid-solution strengthening. This trend was supported by microhardness tests, which revealed significant increases in the transition zones, with peaks reaching up to 373 HV, which is 77.6 % higher than single-material printings.
- Magnetic testing of DED-printed FeSi2.9 showed higher losses relative to laminated FeSi materials, but inductance measurement validated the magnetic saliency of the rotor, demonstrating negligible cross coupling and saturation effects even under high-speed operation.
- The rotor, machined from the bimetallic blank, successfully operated at speeds up to 100 krpm both during centrifugal tests and no-load and load tests when mounted in the motor prototype, with no observed rotodynamic issues. Performance evaluations indicated compliance with the electromagnetic design.

In conclusion, this work confirms the feasibility of using L-DED technology to manufacture high-performance bimetallic rotors. Future studies will focus on refining the fabrication of the bimetallic blank to achieve more precise layer thicknesses. This will include evaluating a hybrid deposition–milling process, aimed at enhancing the magnetic properties and ultimately optimizing the torque ripple of the final component.

CRediT authorship contribution statement

Chiara Gianassi: Writing – original draft, Formal analysis, Data curation. **Erica Liverani:** Writing – review & editing, Supervision, Formal analysis. **Andrea Cavagnino:** Project administration, Funding acquisition. **Luca Zarri:** Validation, Data curation. **Alessandro Ascari:** Resources, Investigation. **Yulong Cui:** Software, Investigation. **Alessandro Fortunato:** Project administration, Funding acquisition, Conceptualization.

Funding

European Union – Next Generation EU.

Declaration of competing interest

The authors declare that they have no known competing financial interests or personal relationships that could have appeared to influence the work reported in this paper.

Acknowledgment

This study was carried out within the «**TUrBO**: the next

100,000+rpm synchronous reluctance motor drives » project – funded by European Union – Next Generation EU within the PRIN 2022 program (D.D. 104 - February 02, 2022 Ministero dell'Università e della Ricerca). This manuscript reflects only the authors' views and opinions, and the Ministry cannot be considered responsible for them.

Nomenclature

E	Specific energy
P	Laser power
v	Scan velocity
D	Laser spot diameter
B	Flux density
H	Magnetic field strength

Data availability

Data will be made available on request.

References

Ascari, A., Lutey, A.H.A., Liverani, E., Fortunato, A., 2020. Laser directed energy deposition of bulk 316L stainless steel. Lasers in Manufacturing and Materials Processing 7 (4), 426–448. https://doi.org/10.1007/s40516-020-00128-w.

Aversa, A., Marchese, G., Bassini, E., 2021. Directed energy deposition of AISI 316L stainless steel powder: effect of process parameters. Metals 11 (6), 932. https://doi.org/10.3390/met11060932.

Cavagnino, A., Vaschetto, S., Pošković, E., Fortunato, A., Liverani, E., 2023. Magnetic behavior and loss assessment of additively manufactured Fe-Si alloys. 2023 IEEE International Electric Machines & Drives Conference (IEMDC), pp. 1–6. https://doi.org/10.1109/IEMDC55163.2023.10238925.

Cestone, L., Melkote, S.N., Liverani, E., Piandoro, S., Ascari, A., Fortunato, A., 2024. The effect of temperature on magnetic properties and surface integrity in $\mathrm{Nd}_2\mathrm{Fe}_{14}\mathrm{B}$ permanent magnets, under dry and wet grinding for automotive applications. Adv. Eng. Mater., 2401200 https://doi.org/10.1002/adem.202401200.

Chen, N., Khan, H.A., Wan, Z., Lippert, J., Sun, H., Shang, S.-L., Liu, Z.-K., Li, J., 2020. Microstructural characteristics and crack formation in additively manufactured bimetal material of 316L stainless steel and Inconel 625. Addit. Manuf. 32, 101037. https://doi.org/10.1016/j.addma.2020.101037.

Credo, A., Kurvinen, E., Petrov, I., Scherman, E., Sopanen, J., Pyrhönen, J., 2023. Materials applicable to an axially-laminated synchronous reluctance machine considering mechanical and electromagnetic aspects. IEEE Trans. Ind. Appl. 1–11. https://doi.org/10.1109/TIA.2023.3309285.

Cui, Y., Gianassi, C., Fortunato, A., Zarri, L., Cavagnino, A., 2024. High-speed synchronous reluctance motors with additively manufactured rotors. 2024 IEEE Energy Conversion Congress and Exposition (ECCE), pp. 5024–5031. https://doi.org/10.1109/ECCE55643.2024.10861406.

Feenstra, D.R., Banerjee, R., Fraser, H.L., Huang, A., Molotnikov, A., Birbilis, N., 2021. Critical review of the state of the art in multi-material fabrication via directed energy deposition. Curr. Opin. Solid State Mater. Sci. 25 (4), 100924. https://doi.org/10.1016/j.cossms.2021.100924.

Garibaldi, M., Ashcroft, I., Lemke, J.N., Simonelli, M., Hague, R., 2018. Effect of annealing on the microstructure and magnetic properties of soft magnetic Fe-Si produced via laser additive manufacturing. Scr. Mater. 142, 121–125. https://doi.org/10.1016/j.scriptamat.2017.08.042.

Garibaldi, M., Ashcroft, I., Simonelli, M., Hague, R., 2016. Metallurgy of high-silicon steel parts produced using selective laser melting. Acta Mater. 110, 207–216. https://doi.org/10.1016/j.actamat.2016.03.037.

Gerada, D., Mebarki, A., Brown, N.L., Gerada, C., Cavagnino, A., Boglietti, A., 2014. High-speed electrical machines: technologies, trends, and developments. IEEE Trans. Ind. Electron. 61 (6), 2946–2959. https://doi.org/10.1109/TIE.2013.2286777.

Gianassi, C., Liverani, E., Ascari, A., Tonoli, A., Cavagnino, A., Fortunato, A., 2025. Characterization of $\mathrm{FeSi}_{2.9}$ and SS 316L Produced by Directed Energy Deposition for Bimetallic High-Speed Rotors. In: Proceedings of the ASME 2025 20th International Manufacturing Science and Engineering Conference, vol. 2. ASME, Greenville, South Carolina, USA. https://doi.org/10.1115/MSEC2025-155456.

Heer, B., Bandyopadhyay, A., 2018. Compositionally graded magnetic-nonmagnetic bimetallic structure using laser engineered net shaping. Mater. Lett. 216, 16–19. https://doi.org/10.1016/j.matlet.2017.12.129.

Jin, Q.-Y., Nam, H., Jo, H., Park, J., Kang, H.J., Kim, D.J., Lee, W., 2024. Design of dissimilar material joint for defect-free multi-material additive manufacturing via laser-directed energy deposition. Heliyon 10 (8), e29666. https://doi.org/10.1016/j.heliyon.2024.e29666.

Khan, S.A., Chivavibul, P., Sedlak, P., Arai, S., Enoki, M., 2013. Analysis of acoustic emission signals during tensile deformation of Fe-Si steels with various silicon contents. Metall. Mater. Trans. 44 (8), 3623–3634. https://doi.org/10.1007/s11661-013-1729-4.

Kurz, W., Bezençon, C., Gäumann, M., 2001. Columnar to equiaxed transition in solidification processing. Sci. Technol. Adv. Mater. 2 (1), 185–191. https://doi.org/10.1016/S1468-6996(01)00047-X.

Lamichhane, T.N., Sethuraman, L., Dalagan, A., Wang, H., Keller, J., Paranthaman, M.P., 2020. Additive manufacturing of soft magnets for electrical machines—A review. Mater. Today Phys. 15, 100255. https://doi.org/10.1016/j.mtphys.2020.100255.

Lee, J., Parmar, A., Shin, Y.C., Zhu, L., 2024. Enhanced magnetic properties and goss texture development of FeSi3.5 by direct energy deposition. J. Mater. Sci. 59 (31), 14510–14529. https://doi.org/10.1007/s10853-024-10016-9.

Li, P., Gong, Y., Xu, Y., Qi, Y., Sun, Y., Zhang, H., 2019. Inconel-steel functionally bimetal materials by hybrid directed energy deposition and thermal milling: microstructure and mechanical properties. Arch. Civ. Mech. Eng. 19 (3), 820–831. https://doi.org/10.1016/j.acme.2019.03.002.

Liu, G., Su, Y., Pi, X., Xin, S., Li, K., Liu, D., Lin, Y.C., 2024. Achieving high strength 316L stainless steel by laser directed energy deposition-ultrasonic rolling hybrid process. Mater. Sci. Eng., A 903, 146665. https://doi.org/10.1016/j.msea.2024.146665.

Murataliyev, M., Degano, M., Di Nardo, M., Bianchi, N., Gerada, C., 2022. Synchronous reluctance machines: a comprehensive review and technology comparison. Proc. IEEE 110 (3), 382–399. https://doi.org/10.1109/JPROC.2022.3145662.

Newman, D., Faue, P., Nishanth, F., Rankouhi, B., Pfefferkorn, F.E., Thoma, D.J., Severson, E., 2023. Solid high-speed synchronous reluctance rotor enabled by multi-material additive manufacturing. 2023 IEEE Energy Conversion Congress and Exposition (ECCE), pp. 3965–3972. https://doi.org/10.1109/ECCE53617.2023.10362787.

Pineau, A., Benzerga, A.A., Pardoen, T., 2016. Failure of metals I: Brittle and ductile fracture. Acta Mater. 107, 424–483. https://doi.org/10.1016/j.actamat.2015.12.034.

Rajamani, D., Vinod, A.R., Reddy, K.N., Kumar, M.S., 2025. Directed energy deposition (DED) of Inconel 718-SS316 L bimetallic structures: experimental investigations and optimization through artificial humming bird algorithm for improved high strain rate and mechanical properties. Results Eng. 25, 104014. https://doi.org/10.1016/j.rineng.2025.104014.

Ribeiro, K.S.B., Mariani, F.E., Coelho, R.T., 2020. A study of different deposition strategies in direct energy deposition (DED) processes. Procedia Manuf. 48, 663–670. https://doi.org/10.1016/j.promfg.2020.05.158.

Sun, K., Li, F., Rong, C., Zuo, L., 2022. Direct energy deposition applied to soft magnetic material additive manufacturing. J. Manuf. Process. 84, 162–173. https://doi.org/10.1016/j.jmapro.2022.10.004.

Tanwar, R.S., Jhavar, S., 2025. Investigation of microstructure and mechanical properties of austenitic steel bimetallic structures fabricated using wire arc direct energy deposition for remanufacturing applications. Journal of Advanced Joining Processes 11, 100287. https://doi.org/10.1016/j.jajp.2025.100287.

Testa, R., Femia, A., Vancini, L., Rizzoli, G., Mengoni, M., Zarri, L., Cavagnino, A., 2024. Open-end winding SyncRel motor drive with a floating capacitor bridge for high-speed applications. 2024 IEEE Energy Conversion Congress and Exposition (ECCE), pp. 6163–6169. https://doi.org/10.1109/ECCE55643.2024.10861457.

Varvolik, V., Wang, S., Prystupa, D., Buticchi, G., Peresada, S., Galea, M., Bozhko, S., 2022. Fast experimental magnetic model identification for synchronous reluctance motor drives. Energies 15 (6), 2207. https://doi.org/10.3390/en15062207.

Vyatskikh, A.L., Wang, X., Haley, J., Zheng, B., Valdevit, L., Lavernia, E.J., Schoenung, J. M., 2023. Residual stress mitigation in directed energy deposition. Mater. Sci. Eng., A 871, 144845. https://doi.org/10.1016/j.msea.2023.144845.

Xiao, Q., Chen, J., Lee, H.B., Jang, C., Jang, K., 2023. Effect of heat treatment on corrosion behaviour of additively manufactured 316L stainless steel in high-temperature water. Corros. Sci. 210, 110830. https://doi.org/10.1016/j.corsci.2022.110830.

Yan, J., Xu, H., Zhang, H., Tang, S., 2009. MoSi2 oxidation resistance coatings for Mo5Si3/MoSi2 composites. Rare Met. 28 (4), 418–422. https://doi.org/10.1007/s12598-009-0081-8.

Zanni, M., Ceschini, L., Fortunato, A., Valli, G., Del Bianco, L., Spizzo, F., 2022. Relationship between microstructure, mechanical and magnetic properties of pure iron produced by laser powder bed fusion (L-PBF) in the as-built and stress relieved conditions. Progress in Additive Manufacturing 7 (6), 1195–1212. https://doi.org/10.1007/s40964-022-00294-7.

Zheng, B., Zhou, Y., Smugeresky, J.E., Schoenung, J.M., Lavernia, E.J., 2008. Thermal behavior and microstructure evolution during laser deposition with laser-engineered net shaping: part II. Experimental investigation and discussion. Metall. Mater. Trans. 39 (9), 2237–2245. https://doi.org/10.1007/s11661-008-9566-6.